Asian Journal of Chemistry; Vol. 35, No. 1 (2023), 239-246

ASIAN JOURNAL OF CHEMISTRY

https://doi.org/10.14233/ajchem.2023.23991

Spray Deposited Ni Doped Co_3O_4 Thin Films for Electrochemical Applications

S.K. JASMIN VIJITHA[1], K. MOHANRAJ[2,3,*] and R.P. JEBIN[1]

[1]Department of Physics & Research Centre, Muslim Arts College, Thiruvithancode-629174, India
[2]Department of Physics, Manonmaniam Sundaranar University, Tirunelveli-627012, India
[3]Department of Physics, School of Basic and Applied Sciences, Central University of Tamil Nadu, Thiruvarur-610005, India

*Corresponding author: E-mail: kmohanraj.msu@gmail.com

Received: 10 September 2022; *Accepted*: 24 December 2022; *Published online*: 27 December 2022; AJC-21104

Nickel-doped Co_3O_4 films were prepared using fluorine doped tin oxide (FTO) substrates at various nickel concentrations (x = 0.025, 0.05, 0.075 and 0.1) using a spray pyrolyzed process at 300 ºC. Experimental techniques were used to characterize the materials by XRD, SEM, EDAX, UV-Vis, FTIR spectroscopy, magnetic susceptibility and cyclic voltammetry. When nickel is present in any concentration of Co_3O_4, the structural analysis using XRD confirms the spinel cubic structure of the material. By using a scanning electron microscope, porous morphological studies are conducted. EDAX examines the chemical composition of the prepared thin films. A 0.050 M concentrations demonstrated the ideal structure, good morphological analysis and energy bandgap. Based on the results, the prepared films were effectively used in the electrochemical performance.

Keywords: Ni-doped Co_3O_4, Thin film, Cyclic voltammetry, Electrochemical studies.

INTRODUCTION

Cobalt oxide is one of the transition metal oxides, which made a promising one for different fields such as smart optical windows, display devices, pigments for glass and ceramics, gas sensors, *etc*. [1-5]. Among these various oxidation states of cobalt, the Co_3O_4 is the most stable compound. Co_3O_4 is widely documented in the literature with desirable electrochemical characteristics [6-8] and spinel crystal structure in the energy storage field [9]. The performance of Co_3O_4 depends upon the microstructure, such as grain size, porosity and crystallinity. Hence, the preparation method is a sensitive one for the overall performance of the compound.

Several synthetic methods are applied for the preparation of Co_3O_4 thin films, *e.g*. chemical method, physical vapour method, chemical vapour deposition, hydrothermal and simple combustion methods [10-16]. Co_3O_4 belongs to a p-type semiconductor and its properties can be changed by doping with an external agents or impurities called dopants [17]. Hence, the selection of a dopant is a vital part of semiconductor doping. It has been challenging to select dopants with a narrow band gap. In present work, nickel is selected as co-dopant, since it acts as the external donar, enhancing the electrical properties [18-21].

EXPERIMENTAL

In this work, precursor materials cobalt(II) nitrate hexahydrate and nickel(II) nitrate hexahydrate, glass and fluorine-doped tin oxide (FTO) substrates were procured from the commercial sources and used as such.

Cleaning of fluorine-doped tin oxide (FTO) substrate: Before usage, the substrates were cleaned using soap and water and then washed thoroughly with acetaldehyde and acetone, then dried overnight at 60 ºC. Following thorough cleaning with soap solution and immersion in chromic acid, the glass substrates were sonicated and then dried in the open air.

Preparation of Ni-doped Co_3O_4: Pure and nickel doped cobalt oxide thin films were prepared by simple spray pyrolysis on substrates such as glass and FTO. Dissolved $Co(NO_3)_2·6H_2O$ in water with ethanol at 1:1 ratio. Then different concentrations of $Ni(NO_3)_2·6H_2O$ (x = 0.025, 0.05, 0.075, 0.1) was added to the former solution and then stirred well for 30 min at room temperature. The mixture solution was sprayed onto the substrate and sintered at 300 ºC.

This is an open access journal, and articles are distributed under the terms of the Attribution 4.0 International (CC BY 4.0) License. This license lets others distribute, remix, tweak, and build upon your work, even commercially, as long as they credit the author for the original creation. You must give appropriate credit, provide a link to the license, and indicate if changes were made.

Characterization: PANanalytical Xpert Pro model XRD (Cu*K*α radiation (λ = 1.54060 ⊕), Perkin-Elmer model FTIR spectrometer (4000 to 400 cm^{-1}), JEOL 6390LA/OXFORD XMX N model SEM/EDAX, Perkin-Elmer lambda 950 model UV-VIS-NIR UV-VIS-NIR spectrophotometers were used to characterize the films. The CH Instrument, model CHI604D electrochemical workstation was used to examine the electrochemical performance of the prepared films using 0.5 M of NaOH electrolyte solution.

RESULTS AND DISCUSSION

XRD studies: The X-ray diffraction patterns of Ni-doped (x = 0.025, 0.05, 0.075 and 0.1) Co_3O_4 thin films are shown in Fig. 1. The temperature used for all thin film depositions was 300 ºC. Multiple diffraction peaks have been found in all films. Strong peaks that were identified include (111), (220), (311), (222), (400), (422), (511), (440), (531), (620) and (533) (622). The preferred peak among these is the peak (311). The appearance of the spinel cubic structure (*Fd*3*m* space group) in nickel-doped and undoped Co_3O_4 was in good accordance with the JCPDS card no. 078-1969. At various nickel concentrations, it is revealed that no nickel cluster parasitic phases are present. This indicates that Ni-doping on Co_3O_4 did not alter its crystalline structure and displays the maximum purity of the prepared films. When nickel was added at various concentrations, the minimal displacement of the diffraction peak was observed. Table-1 shows the structural characteristics of the prepared films at various nickel concentrations. Using Bragg's law, the peak positions can be theoretically calculated using eqn. 1 [22]:

$$d = \frac{a}{\sqrt{h^2 + k^2 + l^2}} \quad (1)$$

where 'd' 'h', 'k' and 'l' refers to interplanar spacing and the Miller indices respectively [23]. For determining accurate unit-cell dimensions from XRD, the systematic errors usually occur due to the X-ray absorption by the specimen and the rotation axis displacement. So some uncertainty exists about the best functions of θ to obtain a linear extrapolation. The lattice parameter value of zero for these extrapolation functions (θ = 90º) gives the actual value of the lattice parameter. Current practice is to plot 'a' against $\cos^2\theta$ to extrapolate linearly to $\cos^2\theta = 0$

$$f(\theta) = \frac{1}{2}\frac{\cos^2\theta}{\sin\theta} + \frac{\cos^2\theta}{\theta} \quad (2)$$

for obtaining fewer errors in the result. From Table-1, the results demonstrated that the structural characteristics for Ni-doped Co_3O_4 at a concentration of 0.050 are in good agreement with those for pure Co_3O_4. This implies that nickel atoms are complately accompanied in the Co_3O_4 lattice space. Moreover, the diffraction peak intensity at the concentration of 0.050, the

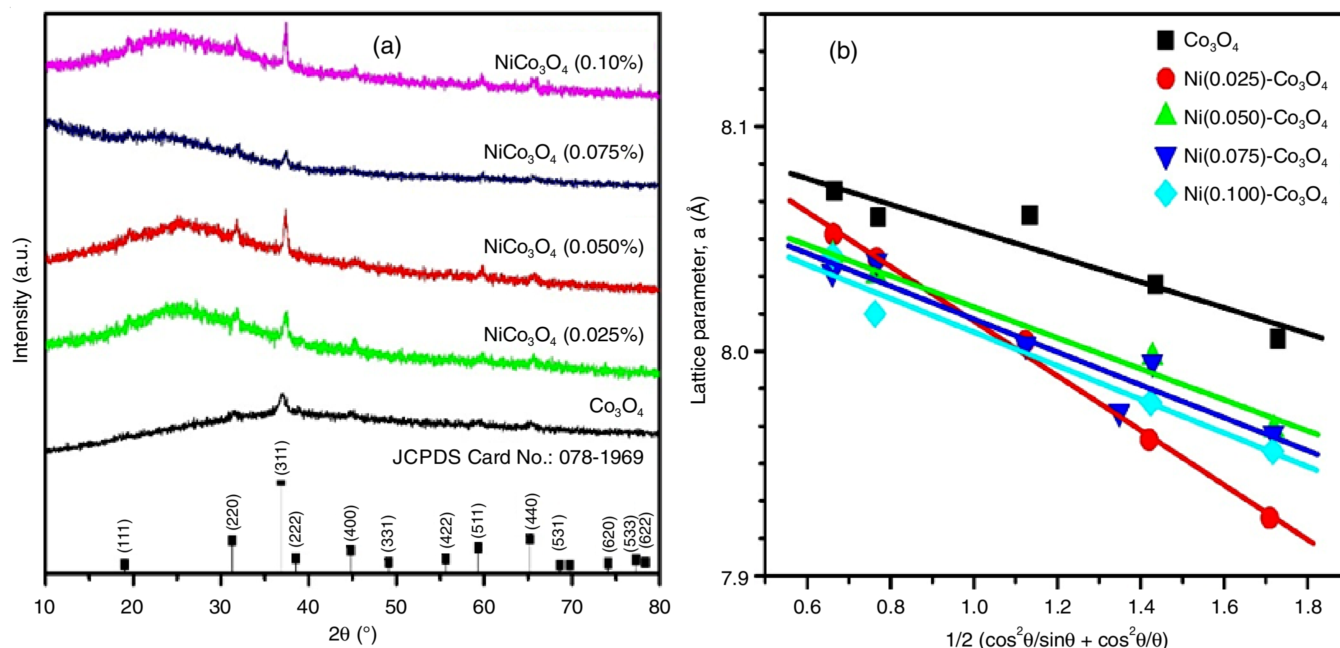

Fig. 1. Co_3O_4 thin films and Ni-doped Co_3O_4 thin films (a) X-ray diffraction patterns and (b) NR plot

TABLE-1
CALCULATED STRUCTURAL PARAMETERS OF Ni-Co_3O_4 THIN FILMS

Ni concentration (x)	Lattice parameter (a) (Å)			Unit cell volume (V) (Å)³		Density (ρ) (gm/cm³)	
	Cal.	N-R Plot	Std.	Cal.	Std.	Cal.	Std.
0.000	8.045	8.111	8.085	518.21	528.49	6.19	6.05
0.025	7.999	8.134		511.9		6.24	
0.050	8.009	8.088		513.9		6.22	
0.075	8.090	8.087		530.28		6.05	
0.100	7.997	8.083		511.62		6.25	

intensity of nickel increased as compared to the other diffraction peaks. Due to the diffraction intensity, the prepared film has a crystalline structure of a higher order than in its natural form. The average crystalline size of the synthesized films was calculated from the Debye-Scherrer's formula [24,25], known as the width increases, crystalline size decreases.

$$D = \frac{K\lambda}{\beta\cos\theta} \tag{3}$$

where 'K' is 0.94, 'λ' is 1.5406 E, 'θ' is the diffraction angle and, 'β' is the FWHM of the peak. Microstrain (ε), dislocation density and stress was calculated using eqns. 4-6:

$$\varepsilon = \frac{\beta\cos\theta}{4} \tag{4}$$

$$\delta = \frac{1}{D^2} \tag{5}$$

$$\sigma = -\left(\frac{E}{2\nu}\right)\left(\frac{d - d_o}{d_o}\right) \tag{6}$$

where 'ε' is Young's modulus (219 MPa), 'ν' is the Poisson's ratio (0.308), 'd' and 'd_o' are d spacing values from the obtained and JCPDS data, respectively. Table-2 shows the calculated values of crystallite size, microstrain, dislocation density and stress of Co_3O_4 thin film samples deposited at various temperatures. The crystalline size of Co_3O_4 film was 22.5 nm, which increased to 46.1 nm, when the nickel concentration increased to 0.05. Further addition of nickel in Co_3O_4 results in a decrease in crystalline size as well as in the microstrain value. Among these, 0.05 doped concentration of nickel in Co_3O_4 shows the most negligible value of microstrain. The reduction in microstrain is due to the displacement of atoms from their ideal positions, making the crystal less imperfect by obtaining the most negligible value in dislocation density. The dislocation density corresponds to the crystal imperfections related to the defective index of the lattice. Moreover, at 0.05 concentration of nickel doped Co_3O_4 shows the minimum stress [26]. The lowest stress value predicts the thin film where molecules are ideally occupied in the crystal phase. It was exceptionally free from the pressure exerted by the external doped nickel atoms.

Morphological studies: The SEM/EDAX images of pure and $Ni_xCo_{3-x}O_4$ (x = 0.025, 0.050, 0.075 and 0.100) films at 300 ºC are shown in Fig. 2a-e. The SEM images of the prepared Ni-doped Co_3O_4 films contain fabricated microspheres. Among these, the surface became more porous as the concentration of 0.05. As a result, the optimized sample that has the most consistent size and structure, which helps to increase the surface area ocobalt oxide. The elemental spectrum analysis confirmed the presence of elements such as Co, Ni, O in the prepared films. As expected, the doping concentration in Co_3O_4 was found to increase in tandem with the composition of nickel.

FTIR studies: FTIR spectra of Co_3O_4 and various Ni-doped Co_3O_4 films are shown in Fig. 3. Two prominent peaks have been identified in the FTIR spectrum of pure cobalt oxide at 895 and 753 cm^{-1} due to vibration of alcohols or phenols in the Co_3O_4 causing the prominent peak to appear at 753 cm^{-1} while the peak at 895 cm^{-1} due to bending vibration of C-O in Co_3O_4. Two other small peaks can be seen at 1368 cm^{-1} and 1742 cm^{-1}, owing to vibrations of amide and carbonyl groups, respectively. The Ni-O-H stretching bond in the prepared Ni-doped Co_3O_4 films is attributed to the absorption band at 619 cm^{-1}. This out-come demonstrates that nickel was successfully added to the Co_3O_4 matrices. Furthermore, similar peaks like 1748, 1353, 876, 761 and 605 cm^{-1} imply the composite's respective peaks of Co_3O_4 molecules.

XPS studies: The XPS spectrum of Ni-doped Co_3O_4 is shown in Fig. 4a. Individual elements such as Co, O, and Ni are present alongside their chemical states. The O1s peak is seen in two spectral lines at 529.9 eV and 531.5 eV (Fig. 4b); which are identified as lattice O and chemisorbed O, respectively. Fig. 4c shows the Co2p spectrum that has peaks at 780.1 eV, 796.3 eV and 787.1 eV, 803.1 eV. The Co^{2+} ions in CoO species are typically found with the observed satellite lines linked to $Co2p_{3/2}$ and $Co2p_{1/2}$. The Ni2p core level spectrum in Fig. 4d has at 854.1 eV and 871.3 eV. In contrast, Ni $2p_{1/2}$ has a binding energy of 871.3 eV, while the $Ni2p_{3/2}$ has binding energy of 854.1 eV.

Optical studies: The UV-vis spectra of the prepared films (200 and 2000 nm) are shown in Fig. 5a-b. It is observed that two absorption edges are seen in the visible region due to the charge transfer of ($O^{2-}\rightarrow Co^{2+}$) and ($O^{2-}\rightarrow Co^{3+}$) in Co_3O_4. The Tauc plots of the prepared thin films at different Ni concentrations is shown in Fig. 6. Two energy band gaps are present in the film [27]; the higher band gap is found to be 1.47 eV due to $O^{2-}\rightarrow Co^{2+}$ charge transfer and the lower band 1.99 eV associated with the $O^{2-}\rightarrow Co^{3+}$ charge transfer [28-30]. The degeneracy of the valence band causes the existence of the two-band gap [31]. By comparing the band gap values, Ni-doped Co_3O_4 is found to be lower at 1.36 eV and 1.76 eV (for 0.050 Ni concentration) which are shifted to pure Co_3O_4. Due to the distortion occurred by the addition of nickel to Co_3O_4 structure, the band gap energy get decreased. As a result, within band gap, impurity levels known as acceptor levels, will arise. Nickel contributes

TABLE-2
THICKNESS, CRYSTALLITE SIZE, MICRO STRAIN, DISLOCATION DENSITY AND STRESS OF Ni DOPED Co_3O_4 THIN FILMS

Ni concentration (x)	Thickness (R_t) (μm)	Debye-Scherrer		Dislocation density δ (× 10^{15} lines/m^2)	Stress σ (MPa)
		Crystallite size (D) (nm)	Microstrain (ε) × 10^{-3}		
0.000	9.62	22.5	1.62	1.99	2.19
0.025	6.00	22.5	1.62	1.97	4.96
0.050	6.92	46.1	0.81	0.47	3.49
0.075	5.68	38.0	0.97	0.69	3.58
0.100	4.77	22.5	1.62	1.97	4.29

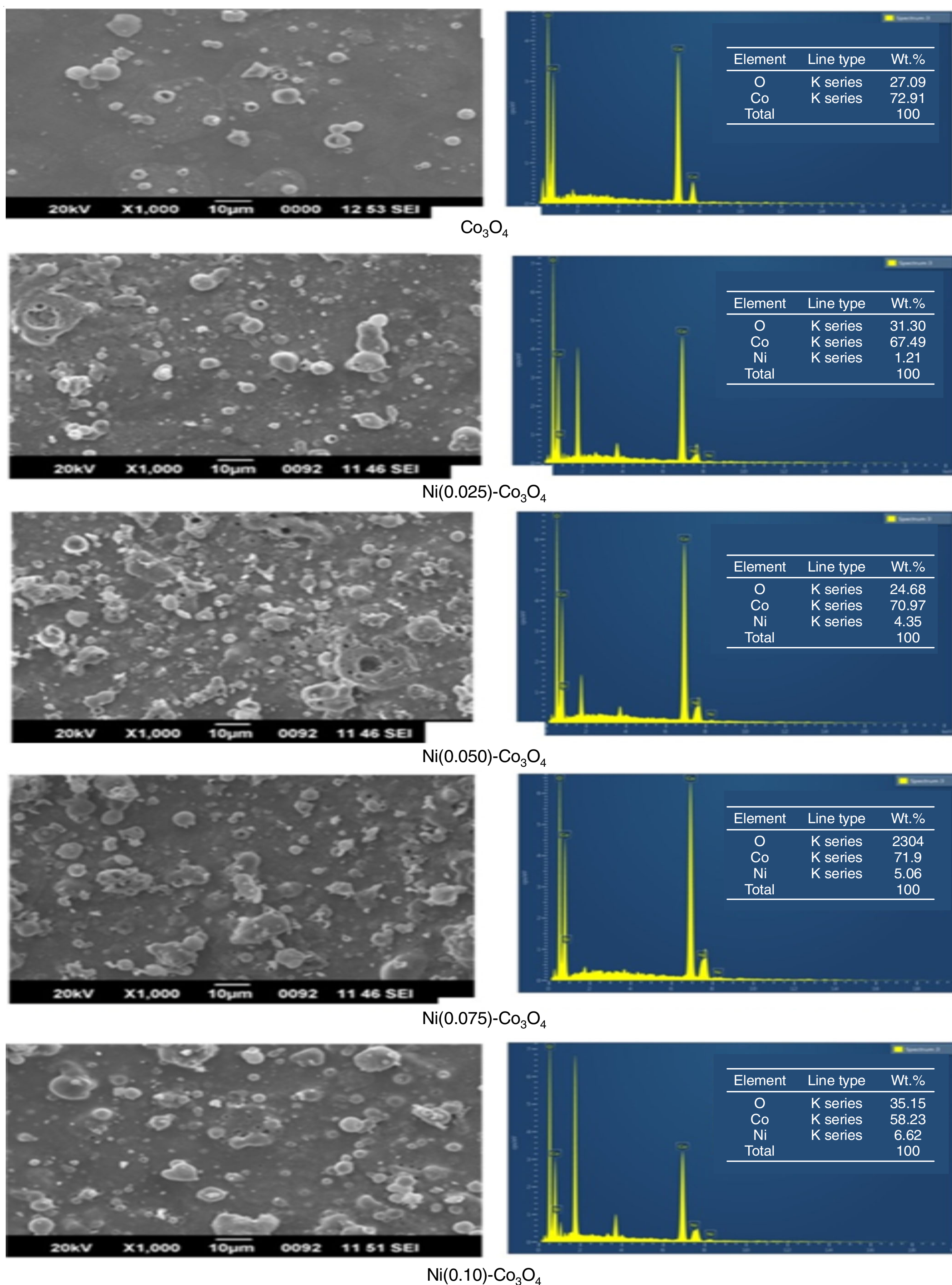

Fig. 2. Scanning electron microscope (SEM) images and elemental analysis spectra of pure and Ni doped Co_3O_4 thin films

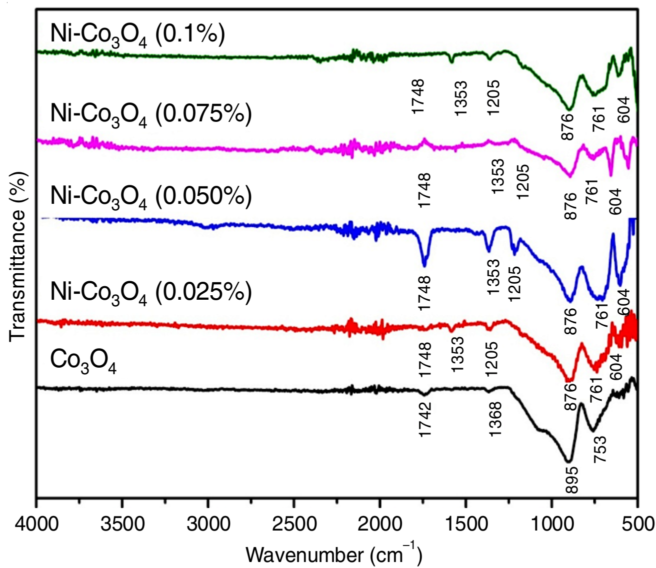

Fig. 3. Fourier transform infrared spectra of pure and Ni doped Co_3O_4 thin films

to the generation of holes (p-type), which would boost the conductivity by acting as charge carriers.

Cyclic voltammetric studies: Fig. 7a shows the cyclic voltammograms (CV) for thin films of Co_3O_4 and Ni-doped Co_3O_4 with potential linear sweeps between -0.1 V and +1.0V at 100 mV/s scan speeds. Two distinct redox peaks were seen at the first anodic potential (0.02 V) and the first cathodic potential (-0.59 V) (dark grey) (Fig. 7a) [32]. Another set of peaks, the second anodic potential (0.38 V) and the second cathodic potential (0.45 V) were observed due to the conversion between Co_3O_4 and CoOOH [33,34]. Similarly, the CV area of voltammograms has increased, indicating that Ni has interacted with Co_3O_4 and directly delivered a higher degree of stored charge and enhanced electrochemical behaviour compared to Co_3O_4 film. The doped films had much higher current densities than pure Co_3O_4 owing to H^+ ion intercalation/de-intercalation into Ni-Co_3O_4 molecules that occurred quickly. This implies that a modest amount of Ni doping in Co_3O_4 matrix provides a simple method for ions diffusion and charge transfer. Moreover, the anodic peak current and cathodic peak current shifted towards positive and negative potential side respectively, as the scan rates increased. A linear increase in CV area and shifting of peak delivers the process is based purely on diffusion-controlled reaction [35], with a significant H^+ ion intercalation and de-intercalation process than Co_3O_4 film.

Fig. 4. (a) XPS spectra of pure and Ni doped Co_3O_4 thin films and (b-d) correspond high resolution spectra

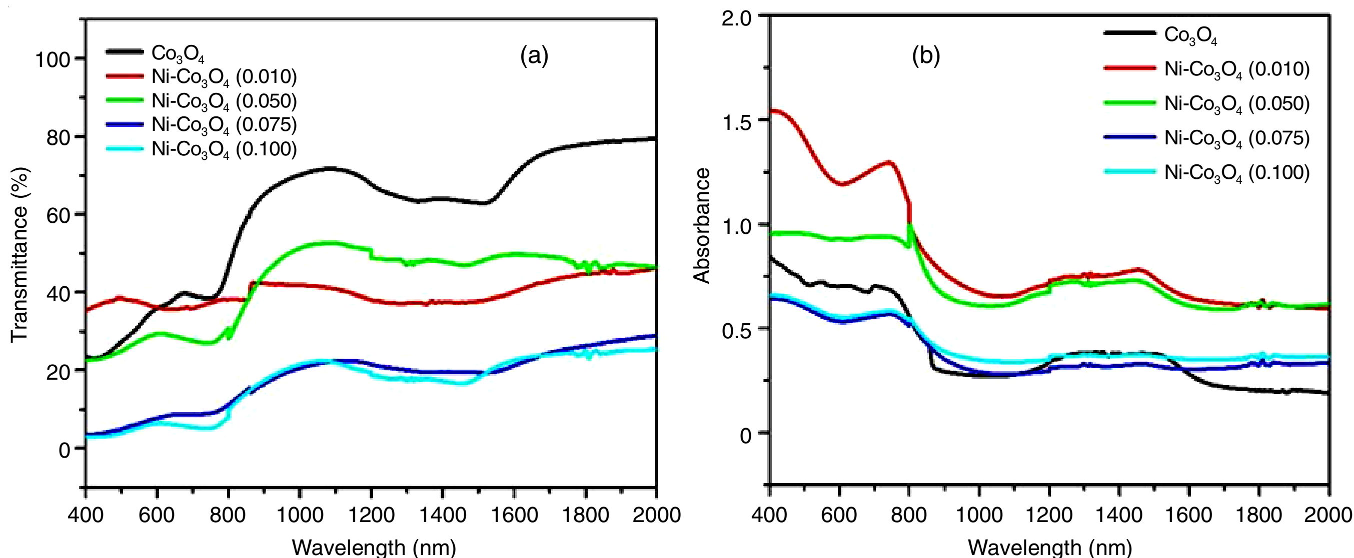

Fig. 5. UV-Vis spectra of (a) pure and (b) Ni doped Co_3O_4 thin films

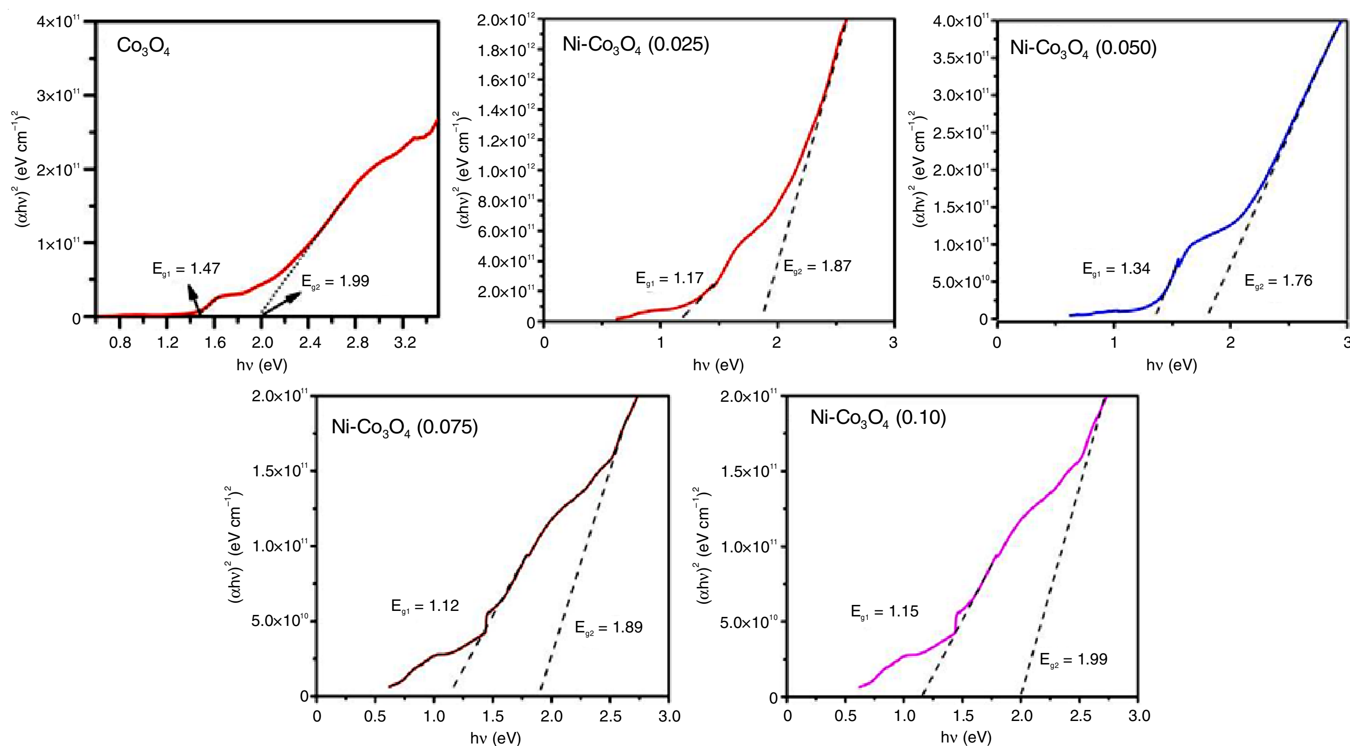

Fig. 6. Tauc plot of Co_3O_4 and Ni doped Co_3O_4 thin films

VSM studies: Fig. 8 shows the vibrating sample magnetometer curve for the prepared films under the magnetic field of –1.5 T to +1.5 T. Pure Co_3O_4 indicates ferromagnetic behaviour and the magnitude of magnetization linearly increases with increasing the applied magnetic field and observed to be 0.004 emu/g. While Ni doping at the Co site diminishes the ferromagnetic nature and leads to super paramagnetic (SPM) behaviour attributed to the double exchange interaction between the nickel ion and structural defects [36,37].

Conclusion

The XRD structural analysis showed that the spinel cubic structure in Co_3O_4 became distorted when nickel was added as a dopant at any point. SEM results revealed that the prepared films have enough porosity structure, which is necessary for the electrochemical applications. The purity of each synthetic film examined by EDAX can be deduced from the elemental data of the film. The successful bandgap reduction was obtained by doping nickel into Co_3O_4 at a concentration of 0.050, as validated by measurements of the UV-visible spectra.

CONFLICT OF INTEREST

The authors declare that there is no conflict of interests regarding the publication of this article.

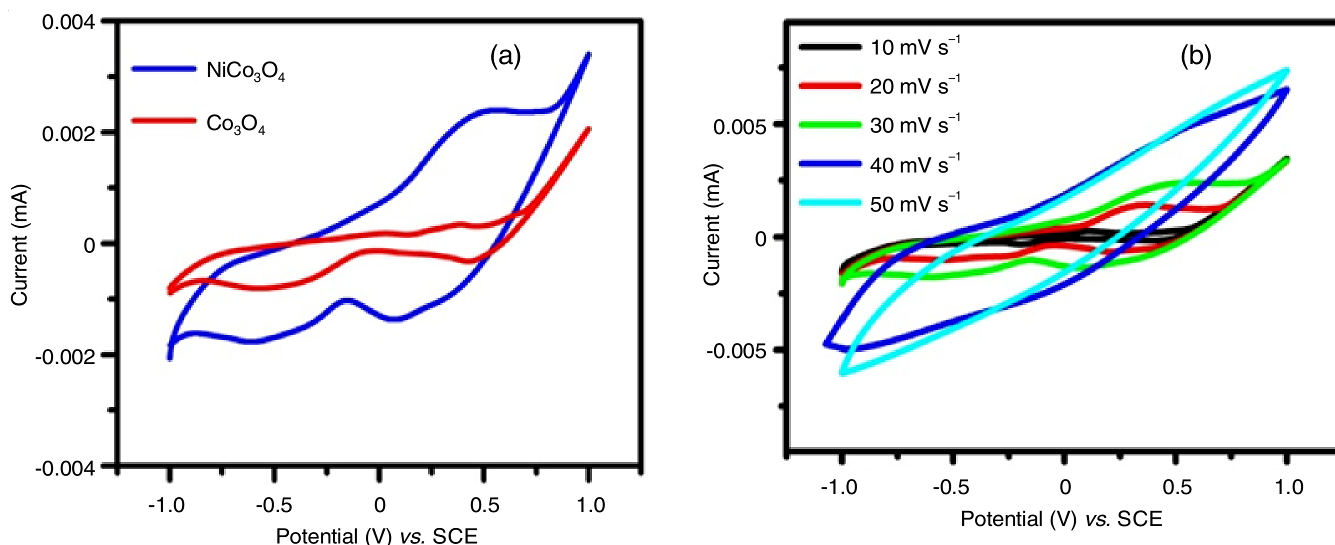

Fig. 7. (a) CV analysis of Co_3O_4 thin film and Ni-doped Co_3O_4 thin films and (b) CV curve of Ni-doped Co_3O_4 thin films at different scan rate

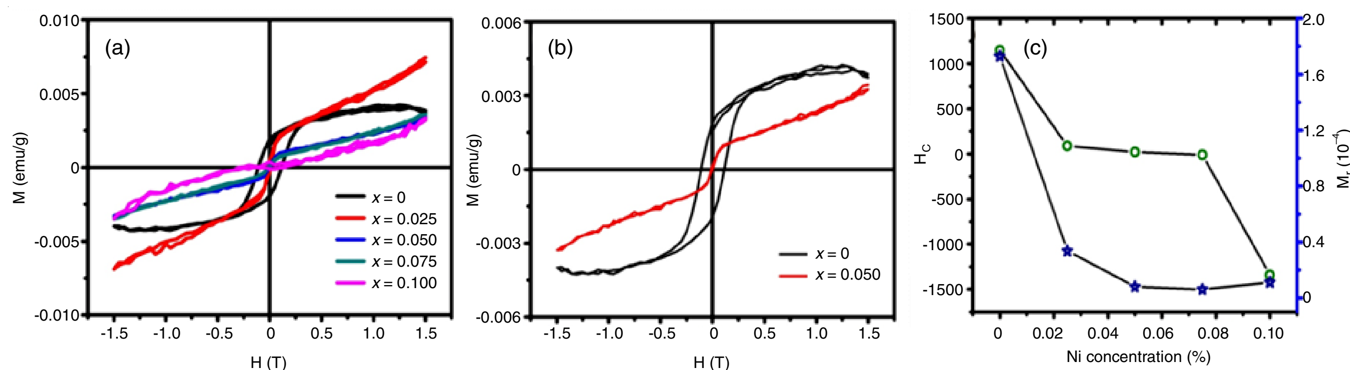

Fig. 8. Isothermal magnetization of (a) pure and (b) Ni doped Co_3O_4, (c) coercivity (H_C) and retentivity (M_r) curve of Ni doped Co_3O_4

REFERENCES

1. J. Cho, M.D. Losego, H.G. Zhang, H. Kim, J. Zuo, I. Petrov, D.G. Cahill and P.V. Braun, *Nat. Commun.*, **5**, 4035 (2014); https://doi.org/10.1038/ncomms5035
2. W.-W. Wang and Y.-J. Zhu, *Mater. Res. Bull.*, **40**, 1929 (2005); https://doi.org/10.1016/j.materresbull.2005.06.004
3. S.J. Uke, V.P. Akhare, D.R. Bambole, A.B. Bodade and G.N. Chaudhari, *Front. Mater.*, **4**, 21 (2017); https://doi.org/10.3389/fmats.2017.00021
4. J. Rajeswari, P.S. Kishore, B. Viswanathan and T.K. Varadarajan, *Electrochem. Commun.*, **11**, 572 (2009); https://doi.org/10.1016/j.elecom.2008.12.050
5. S. Thota, A. Kumar and J. Kumar, *Mater. Sci. Eng. B*, **164**, 30 (2009); https://doi.org/10.1016/j.mseb.2009.06.002
6. L. Yao, Y. Xi, G. Xi and Y. Feng, *J. Alloys Compd.*, **680**, 73 (2016); https://doi.org/10.1016/j.jallcom.2016.04.092
7. H. Razmi and E. Habibi, *Electrochim. Acta*, **55**, 8731 (2010); https://doi.org/10.1016/j.electacta.2010.07.081
8. X. Wang, J. Fu, Q. Wang, Z. Dong, X. Wang, A. Hu, W. Wang and S. Yang, *Crystals*, **10**, 720 (2020); https://doi.org/10.3390/cryst10090720
9. V.R. Shinde, S.B. Mahadik, T.P. Gujar and C.D. Lokhande, *Appl. Surf. Sci.*, **252**, 7487 (2006); https://doi.org/10.1016/j.apsusc.2005.09.004
10. Q. Tang, H. Zhu, C. Chen, Y. Wang, Z. Zhu, J. Wu and W. Shih, *Mater. Res.*, **20**, 1340 (2017); https://doi.org/10.1590/1980-5373-mr-2017-0322
11. I.G. Casella and M. Gatta, *J. Electroanal. Chem.*, **534**, 31 (2002); https://doi.org/10.1016/S0022-0728(02)01100-2
12. J. Wöllenstein, M. Burgmair, G. Plescher, T. Sulima, J. Hildenbrand, H. Böttner and I. Eisele, *Sens. Actuators B Chem.*, **93**, 442 (2003); https://doi.org/10.1016/S0925-4005(03)00168-0
13. S.G. Victoria, A.M.E. Raj and C. Ravidhas, *Mater. Chem. Phys.*, **162**, 852 (2015); https://doi.org/10.1016/j.matchemphys.2015.07.015
14. F. Gu, C. Li, Y. Hu and L. Zhang, *J. Cryst. Growth*, **304**, 369 (2007); https://doi.org/10.1016/j.jcrysgro.2007.03.040
15. J. Pal and P. Chauhan, *Mater. Charact.*, **61**, 575 (2010); https://doi.org/10.1016/j.matchar.2010.02.017
16. Y. Zhang, J. Ge, B. Mahmoudi, S. Förster, F. Syrowatka, A.W. Maijenburg and R. Scheer, *ACS Appl. Energy Mater.*, **3**, 3755 (2020); https://doi.org/10.1021/acsaem.0c00230
17. B.A.D. Williamson, J. Buckeridge, J. Brown, S. Ansbro, R.G. Palgrave and D.O. Scanlon, *Chem. Mater.*, **29**, 2402 (2017); https://doi.org/10.1021/acs.chemmater.6b03306
18. X. Wang, Z. Yang, X. Sun, X. Li, D. Wang, P. Wang and D. He, *J. Mater. Chem.*, **21**, 9988 (2011); https://doi.org/10.1039/c1jm11490e
19. W. Du, R. Liu, Y. Jiang, Q. Lu, Y. Fan and F. Gao, *J. Power Sources*, **227**, 101 (2013); https://doi.org/10.1016/j.jpowsour.2012.11.009
20. L. Yang, S. Cheng, Y. Ding, X. Zhu, Z.L. Wang and M. Liu, *Nano Lett.*, **12**, 321 (2012); https://doi.org/10.1021/nl203600x

21. C. Wang, E. Zhou, W. He, X. Deng, J. Huang, M. Ding, X. Wei, X. Liu and X. Xu, *Nanomaterials*, **7**, 41 (2017); https://doi.org/10.3390/nano7020041
22. C. Ravi Dhas, R. Venkatesh, K. Jothivenkatachalam, A. Nithya, B. Suji Benjamin, A.M. Ezhil Raj, K. Jeyadheepan and C. Sanjeeviraja, *Ceram. Int.*, **41**, 9301 (2015); https://doi.org/10.1016/j.ceramint.2015.03.238
23. S. Desai, M. Suryawanshi, S. Bhosale, J. Kim and A. Moholkar, *Ceram. Int.*, **41**, 4867 (2015); https://doi.org/10.1016/j.ceramint.2014.12.045
24. A. Monshi, M.R. Foroughi and M.R. Monshi, *World J. Nano Sci. Eng.*, **2**, 154 (2012); https://doi.org/10.4236/wjnse.2012.23020
25. P. Bindu and S. Thomas, *J. Theor. Appl. Phys.*, **8**, 123 (2014); https://doi.org/10.1007/s40094-014-0141-9
26. B.D. Cullity and S.R. Stock, Elements of X-ray Diffraction, Pearson New International Edition, Pearson Education Limited (2013).
27. S.G. Kandalkar, J.L. Gunjakar, C.D. Lokhande and O.S. Joo, *J. Alloys Compd.*, **478**, 594 (2009); https://doi.org/10.1016/j.jallcom.2008.11.095
28. S.M. Al-Shomar, *Mater. Res. Express*, **7**, 036409 (2020); https://doi.org/10.1088/2053-1591/ab815b
29. J.P. Jacobs, A. Maltha, J.G.H. Reintjes, J. Drimal, V. Ponec and H.H. Brongersma, *J. Catal.*, **147**, 294 (1994); https://doi.org/10.1006/jcat.1994.1140
30. M. Shelef, M.A.Z. Wheeler and H.C. Yao, *Surf. Sci.*, **47**, 697 (1975); https://doi.org/10.1016/0039-6028(75)90218-6
31. J.I. Pankove, Optical Processes in Semiconductors. Englewood Cliffs: Prentice-Hall (1971).
32. C. Barbero, G.A. Planes and M.C. Miras, *Electrochem. Commun.*, **3**, 113 (2001); https://doi.org/10.1016/S1388-2481(01)00107-2
33. X.H. Xia, J.P. Tu, J. Zhang, X.H. Huang, X.L. Wang and X.B. Zhao, *Electrochim. Acta*, **55**, 989 (2010); https://doi.org/10.1016/j.electacta.2009.09.071
34. A.J. Bard and L.R. Faulkner, lectrochemical Methods: Fundamentals and Applications, John Wiley & Sons: New York, pp. 482-580 (2001).
35. E. Cazzanelli, M. Castriota, R. Kalendarev, A. Kuzmin and J. Purans, *Ionics*, **9**, 95 (2003); https://doi.org/10.1007/BF02376544
36. J. Gupta and A.S. Ahmed, *Physica B*, **599**, 412383 (2020); https://doi.org/10.1016/j.physb.2020.412383
37. S. Gopinath, K. Sivakumar, B. Karthikeyen, C. Ragupathi and R. Sundaram, *Physica E*, **81**, 66 (2016); https://doi.org/10.1016/j.physe.2016.02.006